Geophysical Journal International

Geophys. J. Int. (2012) **189,** 911–922 doi: 10.1111/j.1365-246X.2012.05418.x

Distribution and magnitude of post-seismic deformation of the 2009 L'Aquila earthquake (*M*6.3) surface rupture measured using repeat terrestrial laser scanning

M.W. Wilkinson,[1] K.J.W. McCaffrey,[1] G.P. Roberts,[2] P.A. Cowie,[3] R.J. Phillips,[4] M. Degasperi,[5] E. Vittori[6] and A.M. Michetti[7]

[1] *Department of Earth Sciences, Durham University, UK. E-mail: maxwell.wilkinson@durham.ac.uk*
[2] *Department of Earth and Planetary Sciences, Birkbeck, University of London, UK*
[3] *Department of Earth Science, University of Bergen, Norway*
[4] *School of Earth and Environment, University of Leeds, UK*
[5] *Geological Survey of Trentino, Italy*
[6] *Geological Survey of Italy, High Institute for the Environmental Protection and Research, Rome, Italy*
[7] *Dipartmento di Scienza e Alta Tecnologia, Università dell'Insubria, Como, Italy*

Accepted 2012 February 9. Received 2012 January 17; in original form 2011 July 11

SUMMARY

We captured post-seismic deformation close to the surface rupture of the 2009 L'Aquila earthquake (*M*6.3, central Italy) using repeat terrestrial laser scan (TLS) methods. From 8 to 126 d after the earthquake, we repeatedly laser scanned four road surfaces that intersected the earthquake surface rupture. We modelled vertical near-field deformation, at millimetre-level precision, by comparing subsequent laser scan data sets to the first acquired at each site. The horizontal post-seismic deformation at each site was measured between reflectors paired across the rupture. The TLS data were supplemented by total station data from a fifth site which measured the vertical and horizontal components of post-seismic deformation between two points spanning the rupture. We find post-seismic deformation increased between 44 and 126 d at the southeastern end of the rupture, beneath which a significant gradient in coseismic slip exists within the fault zone. The location, rate of decay and spatially-localized nature of the post-seismic deformation, within tens of metres of the surface rupture suggests it is due to afterslip in the fault zone, driven by increased shear stresses at the edges of regions which slipped coseismically. We note that the magnitude of post-seismic deformation in the far field obtained from InSAR and GPS is not significantly greater than the deformations we have measured close to the rupture. We suggest that shallow, localized afterslip within the fault zone is responsible for the majority of the regional post-seismic deformation field.

Key words: Seismic cycle; Transient deformation; Creep and deformation; Continental neotectonics; Dynamics and mechanics of faulting; Kinematics of crustal and mantle deformation.

1 INTRODUCTION

The 2009 L'Aquila earthquake (M_w 6.3) occurred in the central Italian province of L'Aquila on the April 6 at 3:32 a.m. local time (01:32 UTC). The seismicity was identified to originate from approximately 0.6 to 0.8 m normal sense displacement within a fault zone dipping 54° to the southwest (Walters *et al.* 2009). The Paganica fault, with normal displacement, striking ∼130° N, 6 km east–northeast of the city of L'Aquila was identified as the source of the seismicity. A discontinuous surface rupture was mapped for 2.6 km along the base of the Paganica fault (Vittori *et al.* 2011; Figs 1 and 2). The sharp increase in topographic gradient, which occurs northeastwards across contour 680 m and between sites PA and SP (Fig. 2), indicates the geomorphic expression of the Paganica fault. Each rupture segment displayed a consistent kinematic slip direction of 218° ± 5° (Wilkinson *et al.* 2010). The coseismic offset along these rupture segments was of normal-sense displacement and ranged from hairline cracks with little or no offset to up to 10 cm vertical offset towards the centre of the surface rupture, close to the town of Paganica (Vittori *et al.* 2010).

The L'Aquila earthquake has provided the opportunity for detailed investigation of the magnitude, distribution and rate of decay over time of post-seismic deformation. A study of post-seismic deformation (Amoruso & Crescentini 2009) was conducted at 1400 m depth within the fault zone, using data from two laser strainmeters. The study revealed the propagation of post-seismic slip akin to a diffuse model, while rejecting a model of constant propagation velocity. A study of surface faulting by Boncio *et al.* (2010), revealed

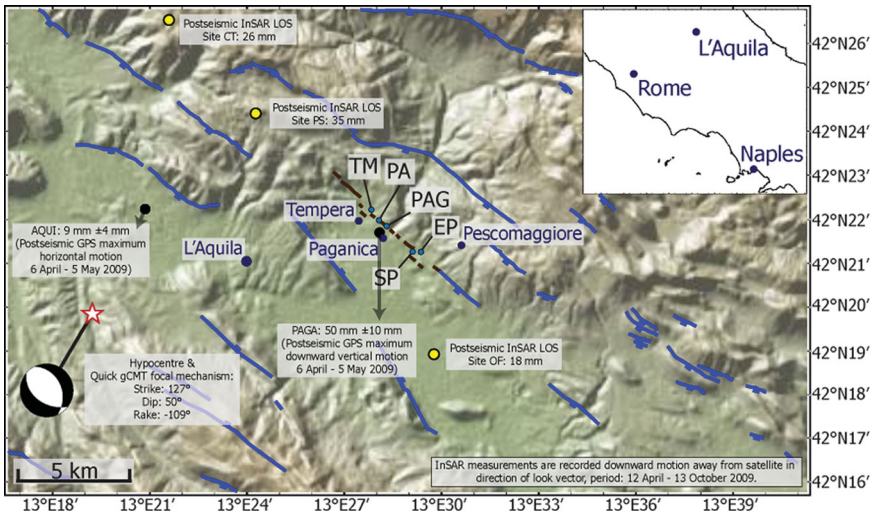

Figure 1. Map of the interpreted active normal faults of the L'Aquila region, and the five study sites PAG, SP, EP, TM and PA. The L'Aquila earthquake surface ruptures are shown in brown (adapted from Michetti *et al.* 2000; Roberts 2008; Falcucci *et al.* 2009; Vittori *et al.* 2011). Additional post-seismic data in the far field from D-InSAR is obtained from Lanari *et al.* (2010). The post-seismic GPS data is from Cheloni *et al.* (2010).

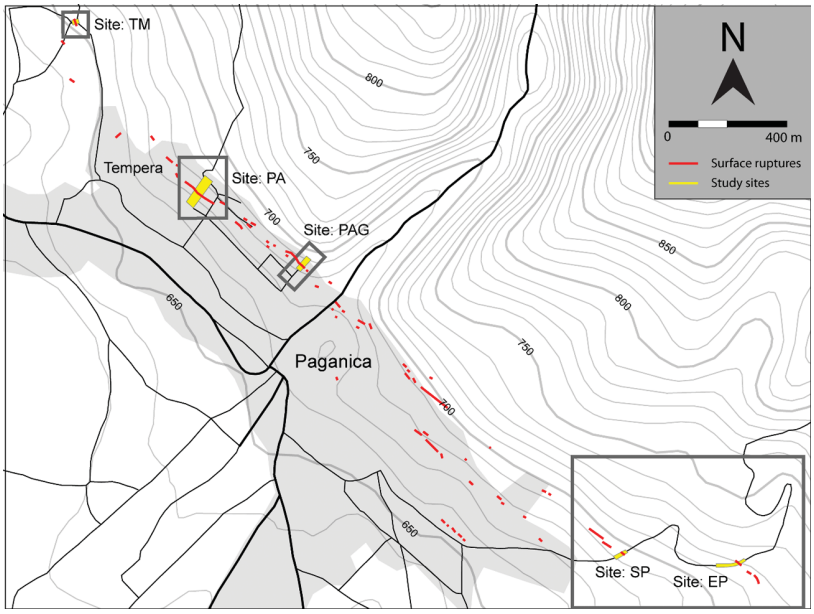

Figure 2. Regional topographic map, detailing the location of the five study sites in yellow. The mapped surface ruptures shown in red after Vittori *et al.* (2011). Black lines represent major and minor roads. The grey shading shows the extent of the urban area around the town of Paganica and its suburbs. Topographic contours are shown in dark grey with a 10 m interval. The boxes around each study site refer to the coverage of the site maps in Fig. 3.

the first evidence of near-field post-seismic deformation immediately after the earthquake. They observed widening of ground fractures by 2 cm between April 6 and April 25 and the deformation of a hangingwall flexure 2.5–3 m wide which opened by 4–5 cm and was vertically offset by ∼2.5 cm. The component magnitudes and rate of decay of post-seismic deformation in the far field were computed by Cheloni *et al.* (2010), who produced an inversion model of the fault zone from two GPS stations (AQUI and PAGA, Fig. 1). They showed that afterslip occurred in regions at the periphery of coseismic slip where increased shear stress is produced by large gradients in coseismic slip, driving afterslip in regions of the fault zone, which did not slip coseismically. A DInSAR analysis of post-seismic displacements in the far field was conducted by Lanari *et al.* (2010). The hangingwall of the Paganica fault was found to be actively deforming with decay times comparable to those of afterslip within the fault zone, suggesting the far-field deformation was driven by fault zone processes. The study identified post-seismic deformation, which was greatest and decayed more rapidly in three discrete regions (PS, CT and OF, Fig. 1).

In this study, we investigate the along-strike distribution and magnitude of post-seismic deformation using repeat Terrestrial Laser Scan (TLS) data sets at four sites (Figs 1 and 2: TM, PAG, SP and EP) spanning the extent of the surface rupture of the Paganica fault, as defined by Vittori *et al.* (2011). We complement these data with that of across-rupture total station measurements from a fifth site (Figs 1 and 2: PA). This multisite approach expands on the previous single-site repeat-TLS study (Wilkinson *et al.* 2010) and provides an insight into the along-rupture magnitude and distribution of post-seismic deformation. Our measurements are confined to surface deformation in the near field within a few tens of metres of the surface

rupture. We compare the magnitude of post-seismic deformation measured in the near-field to far-field values measured from studies of GPS (Cheloni *et al.* 2010) and DInSAR (Lanari *et al.* 2010) to suggest post-seismic deformation on all scales is driven by afterslip within a discrete fault zone. Using measurements of near-field on-rupture post-seismic deformation we provide further evidence to suggest post-seismic deformation within the fault zone occurs in specific regions, which experienced increased shear stresses due to large gradients in coseismic slip.

2 METHOD

Terrestrial Laser Scanning is a ground-based light detection and ranging (LiDAR) technology, which enables exceptionally high-resolution 'point cloud' 3-D digital topography to be acquired, dependent on the machine specification, at lines of sight up to 2 km from the scanner. TLS is often used to document and characterize primary and secondary site effects in earthquake-damaged regions for geological and geo-engineering purposes. Recent examples include reconnaissance reports from the Nigata, Chile, Sendai and Haiti earthquakes by the GEER Association, visualization of surface and structural deformations from the 2004 Nigata earthquake (Kayen *et al.* 2006) and detailed rupture-offset mapping using TLS after the 2010 El-Mayor-Cucapah earthquake (Gold *et al.* 2010).

TLS technology can also be used for detection of change in areas of active deformation, with subtle changes in the geometry of the data sets used to model and infer the resultant deformation occurring between the acquisition of one data set and the next. We employ such an approach in this study to ascertain the magnitude and along rupture distribution of post-seismic deformation at four sites on the surface rupture of the L'Aquila earthquake. A Riegl LMS-z420i terrestrial laser scanner (RIEGL Laser Measurement Systems GmbH, Horn, Austria) was used to acquire a total of twenty three point cloud data sets between 8 and 126 d after the L'Aquila earthquake over four road sites (Table 1; Figs 1 and 2: PAG, SP, EP and TM) cross-cut by the surface rupture of the L'Aquila earthquake. The laser scanner was set up in a level orientation over the same benchmark (Fig. 3: Scan positions) at each site and the point cloud data set collected during each occupation comprised a single scan of the road surface. The relatively short range of the area studied from the scan position (up to 50 m) allowed us to collect data sets with very high spatial density (point spacing of 4–10 mm). The laser scan data sets were corrected for changes in air temperature and pressure between successive scans. When using the Riegl LMS-z420i laser scanner, a fluctuation of either $+20$ °C in air temperature or –70 mBar in air pressure produce a change of $+20$ ppm in the range measurement ($+1$ mm for a range measurement at 50 m). Changes in relative humidity are negligible. An increase of $+90$ per cent in relative humidity at 20 °C air temperature and 1000 mBar air pressure increases the range measurement by $+0.8$ ppm. A semi-permanent fixed network of cylindrical reflectors were used at each site to position subsequent point cloud data sets into a preliminary footwall static reference frame relative to the initially acquired point cloud using the Riegl RiSCAN registration software. The point cloud data sets were individually interpolated within GoCAD to produce representative road surfaces for each point cloud data set using the discrete smooth interpolation (DSI) method (Mallet 1992). The DSI method aims to produce an interpolated surface with the smoothest profile possible, while still honouring the input point cloud. The DSI method is particularly suited to produce representative surfaces of essentially smooth features such as road surfaces, as the method omits small-scale noise inherent to the point cloud from the final interpolated surface. Discrete offsets in the road surface due to earthquake rupturing were preserved by interpolating the footwall and hangingwall as separate surfaces. After surface creation, the reflector-calculated preliminary footwall static reference frame is refined. The refinement involves rotating each of the subsequently acquired pointset surfaces such that their footwall surface triangle vertices colocate with those of the initially acquired pointset surface. This surface-to-surface refinement procedure ensures modelled differences in the hangingwall are due to post-seismic deformation and not misalignment of the point clouds. The vertical component of post-seismic deformation was measured by calculating the vertical difference between correspondingly paired triangle vertices of the initial and subsequent surfaces. By seeding each DSI interpolation using a common initial surface and boundary condition, all corresponding triangle vertices from each of the surfaces were created such that only a vertical difference existed between them. The map spacing between neighbouring vertices was set to 10 cm, which is far greater than the horizontal post-seismic deformation measured at the sites. This approach ensured that lateral differences did not exist between vertices, which could upset the calculation of true vertical difference. Each vertical difference calculated between vertices represents the vertical component of surface deformation, which occurred between the acquisitions of the two data sets, at a unique position on the road surface. The calculated vertical differences can be colour-mapped onto the surface (Figs 4a–7a). Cross-sectional plots of the deformation, perpendicular to the main strike of the rupture were produced for each site using a moving point average with window size of 250 points using the vertical difference values for each site (Figs 4b–7b). The moving window represents 3 m width $\times$ 0.7 m distance along the road at site PAG, 6 m $\times$ 0.35 m at site SP, 9 m $\times$ 0.23 m at site EP and 4 m $\times$ 0.52 m at site TM. The cylindrical reflectors at each location also enabled us to measure horizontal deformation by comparing the change in horizontal distance between reflector sites paired across the rupture relative to their initial distance during the acquisition of the first data set.

3 RESULTS

3.1 Site: PAG

Site PAG, towards the centre of the surface rupture (Fig. 2) is situated on a rough concrete road on the outskirts of Paganica (Fig. 3c) and has been described previously by Wilkinson *et al.* (2010), but is included here for completeness. The surface rupture cross cuts the concrete road with a NW–SE strike and an initial vertical displacement of $\sim$7.5 cm observed 8 d after the earthquake. The TLS data acquired at the site consists of seven repeat scans acquired at 8, 11, 35, 39, 43, 48 and 124 d after the earthquake (Table 1). The scan data was cropped to cover a 3 m $\times$ 65 m section of the road that spans the hangingwall, rupture and footwall of the Paganica surface rupture. The results of the surface generation and vertical difference measurements describe surface deformation, which are partitioned between afterslip on the rupture and the progressive development of a growing hangingwall trough (Fig. 4). The boxed zone in Fig. 4(b) highlights an area of damage (breaking off of the footwall) the surface rupture received between days 11 and 35 attributed to a vehicle being driven over it. The similarity of the deformation observed along the rest of the road before and after the vehicle damage shows that the immediate 2–3 m of footwall was the only part of the road which was damaged. Both the rupture afterslip and the hangingwall

Table 1. Survey dates and measurements of rupture throw, hangingwall trough subsidence, combined rupture throw and hangingwall trough subsidence and horizontal line of sight extension between reflectors for each of the five data sets, relative to the first measurement acquired at each site.

Date	Data set ID	Location (lat/long)	Days since earthquake	Rupture throw since first data set (mm)	Hangingwall trough subsidence since first data set (mm)	Combined rupture throw and hangingwall trough subsidence since first data set (mm)/Site PA: total vertical deformation (mm)	Horizontal line of sight extension between reflectors since first data set (mm)
2009 April 14	PAG 1	13.471450°E 42.362631°N	8	–	–	–	–
2009 April 17	PAG 2		11	2.2	11.6	13.8	11.4
2009 May 11	PAG 3		35	3.9	19.5	23.4	15.9
2009 May 15	PAG 4		39	4.1	19.4	23.5	9.3
2009 May 19	PAG 5		43	5.2	17.3	22.5	16.4
2009 May 24	PAG 6		48	8.3	16.2	24.5	17.2
2009 August 08	PAG 7		124	13.4	14.3	27.7	21.8
2009 April 17	SP1	13.484543°E 42.354447°N	11	–	–	–	–
2009 May 14	SP2		38	6.8	2.7	9.5	7.2
2009 May 18	SP3		42	7.3	3.3	10.6	16.5
2009 May 21	SP4		45	8.0	3.3	11.3	19.7
2009 August 10	SP5		126	13.1	2.9	16.0	27.6
2009 April 16	EP1	13.489044°E 42.354056°N	10	–	–	–	–
2009 May 14	EP2		38	3.3	−3.1	0.2	14.3
2009 May 18	EP3		42	3.4	−2.2	1.2	15.9
2009 May 22	EP4		46	4.5	−2.2	2.3	10.5
2009 August 09	EP5		125	10.8	4.6	15.4	20.3
2009 April 18	TM1	13.462563°E 42.370022°N	12	–	–	–	–
2009 May 13	TM2		37	0.6	–	–	−4.8
2009 May 17	TM3		41	0.9	–	–	4.2
2009 May 20	TM4		44	1.7	–	–	2.9
2009 May 23	TM5		47	1.9	–	–	1.4
2009 August 08	TM6		124	2.4	–	–	3.2
2009 April 23	PA1	13.467295°E 42.364682°N	17	–	–	–	–
2009 May 05	PA2		31	–	–	3.1	5
2009 May 20	PA3		44	–	–	7.8	6.3
2009 June 10	PA4		65	–	–	10.8	6.8
2009 June 30	PA5		85	–	–	11.7	12.5
2009 July 29	PA6		114	–	–	13.8	10.1

trough continued to develop with a decaying rate until the end of our survey (Fig. 8a). The maximum rupture afterslip totalled 13.4 ± 2.6 mm. The maximum observed subsidence in the hangingwall trough was 14.3 ± 2.3 mm. The maximum vertical post-seismic deformation observed was 27.7 ± 2.3 mm, from the combined rupture afterslip and hangingwall trough subsidence. The network of five reflector positions (R1–R5, Fig. 3c) were used to calculate the horizontal component of post-seismic deformation, which totalled 21.8 ± 5.0 mm for the 8–124-d period after the earthquake.

3.2 Site: SP

Site SP is situated towards the southeastern end of the surface rupture (Fig. 2), on the tarmac road from Paganica to Pescomaggiore (Fig. 3a). The rupture is defined by a 5–50 cm wide zone of small cracks, striking NE–SE. The cracks were 2–5 mm wide with no apparent vertical displacement when first observed 11 d after the earthquake. Five scans were acquired at 11, 38, 42, 45 and 126 d after the earthquake, spanning an area 6 m × 49 m encompassing the hangingwall, surface rupture and footwall. Surface fitting and vertical differencing show progressive hangingwall subsidence indicative of rupture afterslip, accompanied by the initial development of a trough in the immediate hangingwall of the rupture (Fig. 5). Rupture afterslip was measured with respect to the first scan datum and inferred by projecting the hangingwall surface of each data set into the rupture zone. The maximum afterslip 126 d after the earthquake was 13.1 ± 4.1 mm, calculated from the difference between scan SP1 and SP5. The hangingwall trough developed between data sets SP1 and SP2 (11–38 d), representing 2.7 ± 2.2 mm of vertical subsidence. Further significant growth of the trough was not observed after 38 d. The maximum vertical post-seismic deformation is 16.0 ± 2.2 mm. This figure represents the sum of the afterslip observed between the first and last data acquisitions (13.1 mm), plus the observed subsidence of the hangingwall trough (2.7 mm) over the same period. A network of four reflectors (Fig. 3a, Rs1–Rs4) paired across the rupture moved 27.6 ± 5.0 mm horizontally in the direction of the coseismic slip vector (218°) between SP1 and SP5. The components of post-seismic deformation of each surface relative to the first are shown in Fig. 8(b); they describe deformation increasing at a decaying rate, indicative of afterslip and near-field post-seismic deformation.

3.3 Site: EP

Site EP is located 370 m due east of site SP on the road from Paganica to Pescomaggiore (Fig. 2). The appearance of the rupture is very similar to that at SP, defined by a narrow zone of cracks crossing the road. The cracks had horizontal displacements of 2–5 mm, but no

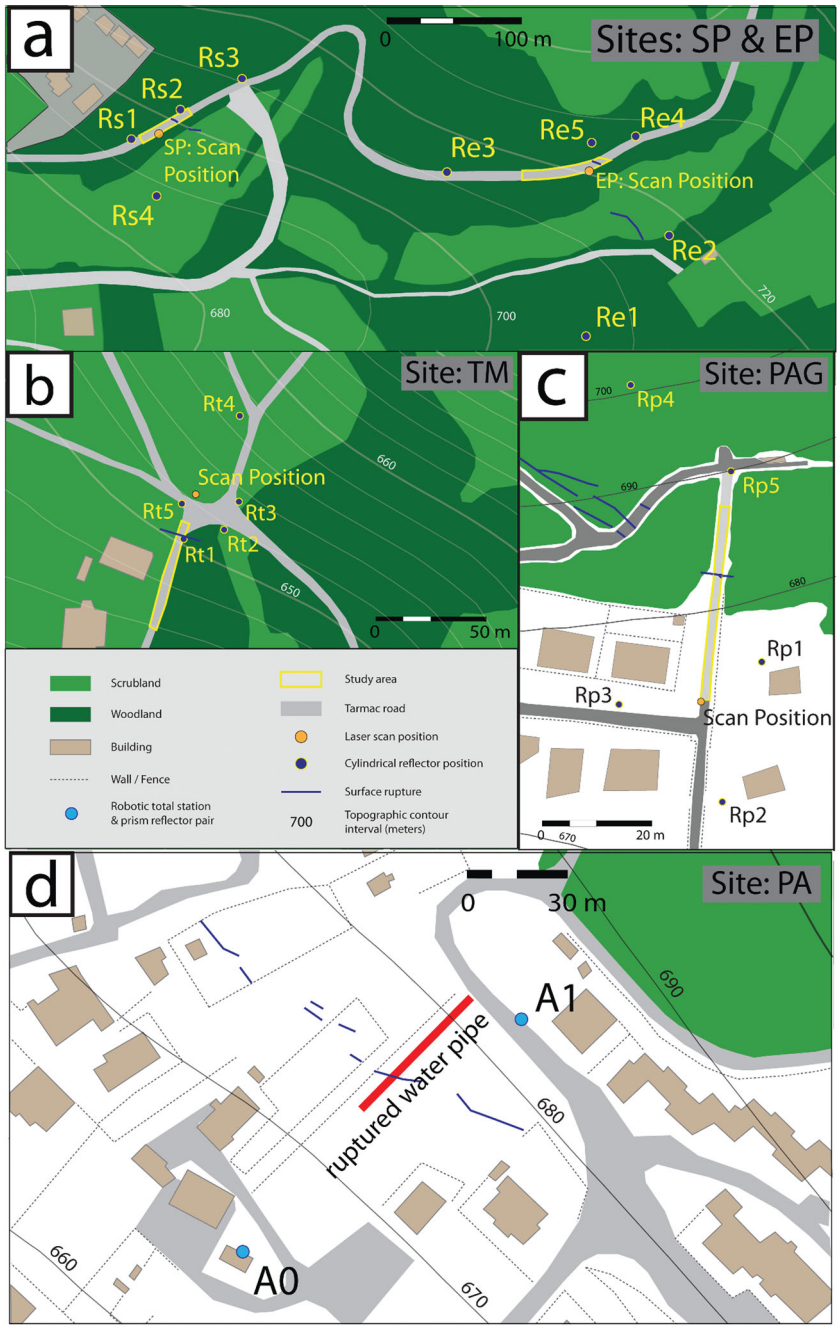

Figure 3. (a–d) Local maps for sites SP and EP, TM, PAG and PA. Land use depicts line of sight restrictions on the reflector network and the extent of the study areas.

vertical displacement observable to the eye in the field. Five scans were acquired at 10, 38, 42, 46 and 125 d after the earthquake of a 9 m × 84 m area, comprising the hangingwall, rupture and footwall. Surface generation and vertical differencing show a trough within the first 4 m of the hangingwall (Fig. 6b: −18 m to −22 m distance from the scanner) that developed between scans EP1 and EP2, along with tilting of the hangingwall towards the rupture between 4 and 50 m from the rupture (−18 m to 50 m distance from the scanner). Hangingwall tilting was contemporaneous with uplift of up to 20 mm at 72 m from the rupture (50 m distance from the scanner). A period of quiescence followed, with little or no change in the surface between EP2 and EP4, except for 2 mm subsidence of the hangingwall from its tilted position. The final scan EP5, acquired 125 d after the earthquake shows significant downthrow of the entire hangingwall by 10.8 ± 3 .8 mm relative to EP1, with additional subsidence of 4.6 mm, creating a hangingwall trough 48 m from the rupture (5–50 m distance from the scanner; Fig. 6b). 10.8 mm of afterslip was observed between 10 and 125 d by projecting the tilted hangingwall into the rupture. The combined magnitude of vertical post-seismic deformation between 10 and 125 d is 15.4 ± 3.1 mm, representing the sum of the maximum afterslip observed (10.8 mm) combined with the observed subsidence of the hangingwall trough (4.6 mm) over the same period. A network of five reflectors (Re1–Re5, Fig. 3a) paired across the rupture were used to measure a horizontal deformation of 20.3 ± 5.0 mm, between 10 and 125 d, resolved in the direction of the coseismic slip vector.

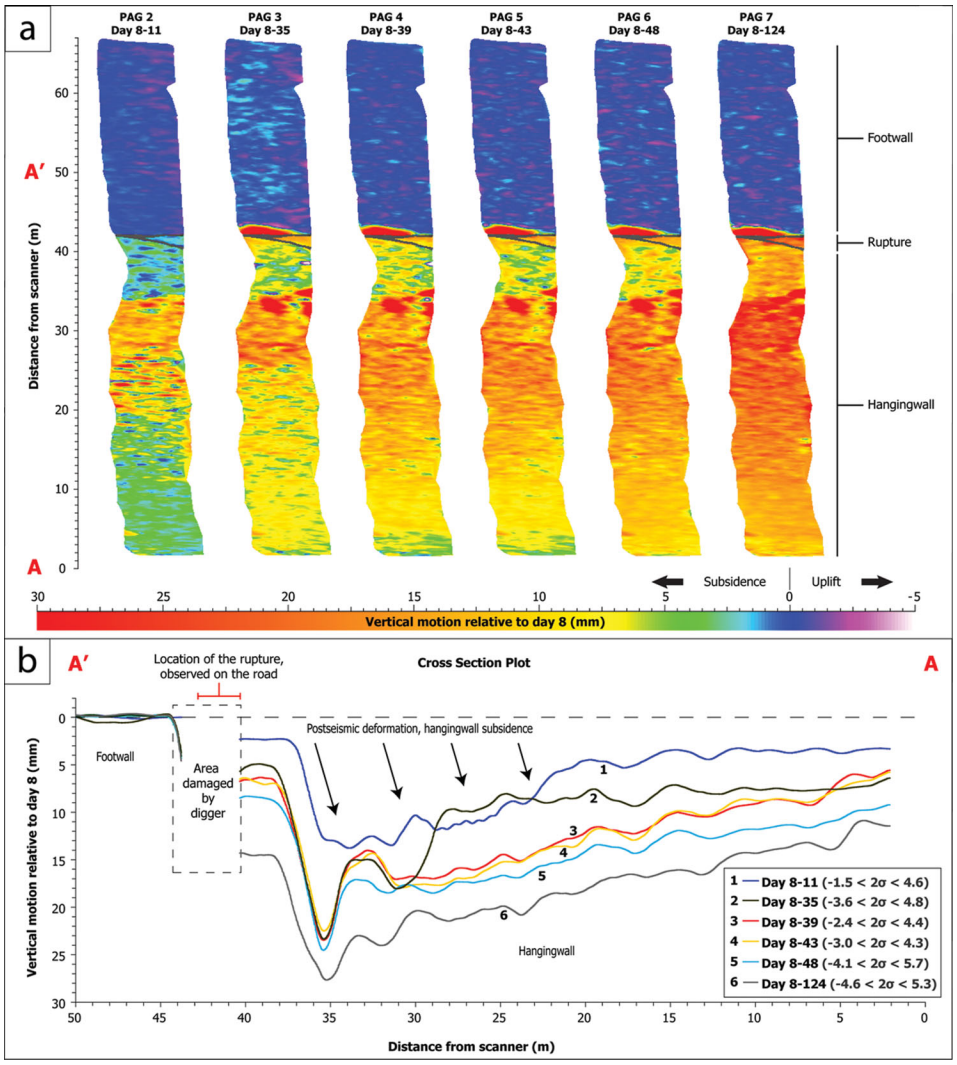

Figure 4. Post-seismic deformation result for site PAG. (a) Colour map plot of vertical deformation (mm) in a footwall static reference frame for subsequent TLS data sets, relative to the initial data set acquired at the site. (b) Cross-sectional plot of the surface deformation between A and A' in (a).

The components of post-seismic deformation of each surface relative to the first are shown in Fig. 8(c). They describe deformation increasing at a decaying rate, indicative of afterslip and near-field post-seismic deformation.

3.4 Site: TM

Site TM is located towards the northwest end of the surface rupture, on the outskirts of the village of Tempera (Fig. 2). The study site is a rough tarmac road (Fig. 3b), 4 m × 51 m, comprising the Paganica surface rupture, hangingwall and footwall. The surface rupture consists of a single crack cross cutting the tarmac road. As observed 12 d after the earthquake, the crack had a horizontal displacement of 8–12 mm, with no vertical offset observable by eye in the field. The site was scanned six times, (12, 37, 41, 44, 47 and 124 d) after the earthquake (TM1–TM6, Table 1). Surface fitting and vertical differencing revealed vertical deformations mostly below the precision of the method (Fig. 7: -2.8 mm $< \pm 2\sigma <$ 2.8 mm), suggesting that minimal vertical post-seismic deformation occurred at the site. Most of the vertical deformations are, however, downward and appear to create a subtle depression in the hangingwall between 33 and 63 m distance from the scanner. Values for rupture afterslip were calculated using the vertical deformation of the road in the immediate hangingwall of the rupture. The maximum observed afterslip was 2.4 ± 2.8 mm, occurring between 12 and 124 d after the earthquake. A network of five reflectors paired across the rupture was used to calculate the horizontal component of post-seismic deformation. The horizontal post-seismic deformation observed between 12 and 124 d was 3.2 ± 5.0 mm. The components of post-seismic deformation over the survey period (Fig. 8d) describe deformations below the precision of the method, suggesting little or no post-seismic deformation occurred at this site.

3.5 Site: PA

Site PA is located 400 m northwest of site PAG (Fig. 2). A 40 bar water pipe crosses the Paganica fault at this site and ruptured during the April 6 earthquake and also subsequently, following repair, at 06:00 on April 19. The immediate area of the water pipe was heavily excavated by water leaking the pipe at high pressure following rupture during the April 6 earthquake. Although those sediments, which may have been ruptured, were washed away, surface ruptures remain in the immediate area along strike with coseismic displacements of 10–15 cm (Vittori *et al.* 2011). At this site, we summarize

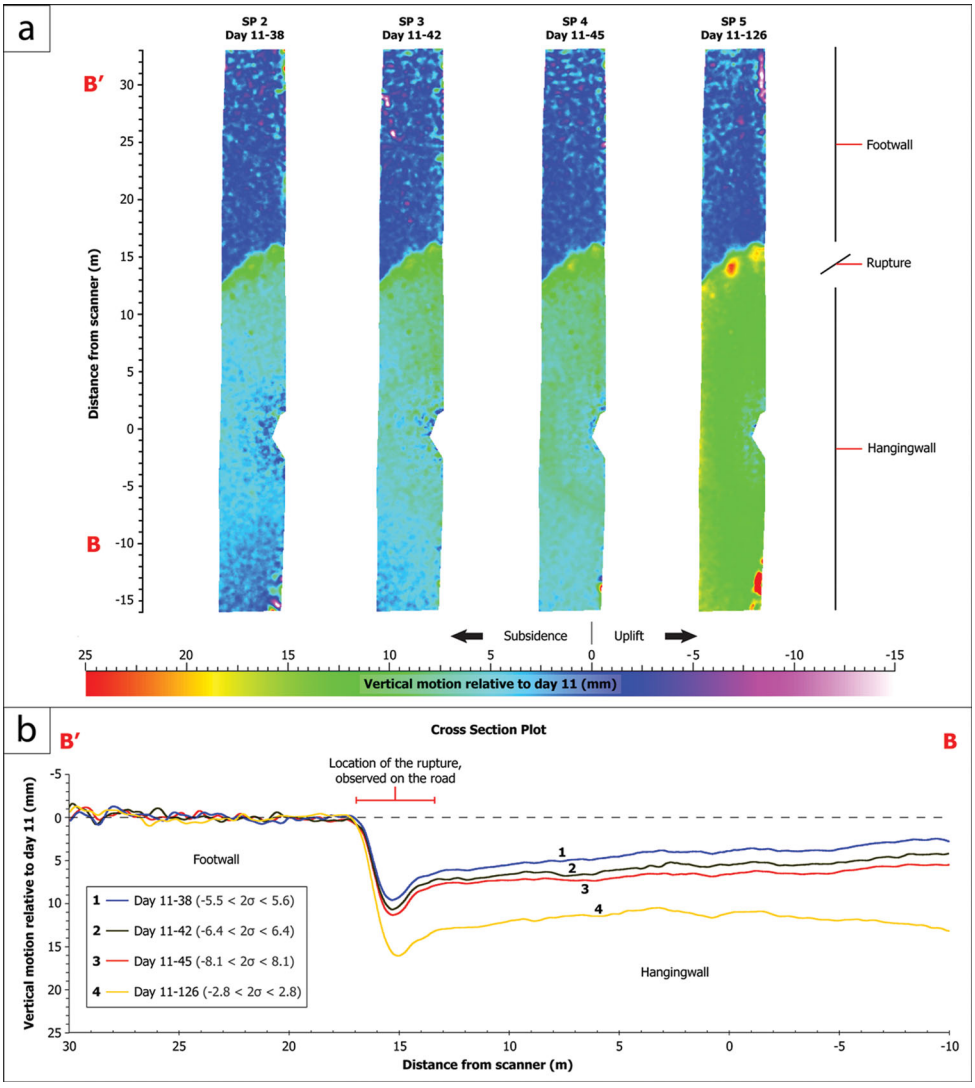

Figure 5. Post-seismic deformation result for site SP. (a) Colour map plot of vertical deformation (mm) in a footwall static reference frame for subsequent TLS data sets, relative to the initial data set acquired at the site. (b) Cross-sectional plot of the surface deformation between B and B' in (a).

data (with permission) from the Geological Survey of Trentino (Degasperi 2010). The Geological Survey installed a Leica TCA2003 automatic total station 63 m in the hangingwall of the rupture (Fig. 3d: point A0). The total station was paired with a staked prism 40 m in the footwall (Fig. 3d: point A1) and set to record the distance to the prism at regular intervals with a precision ± 1.1 mm (1.0 mm +1ppm over ∼100 m distance). The vertical and horizontal components of post-seismic deformation between 17 and 330 d after the earthquake were calculated by comparing subsequent vertical and horizontal distances to the initial measurement. We use the six measurements from 17, 31, 44, 65, 85 and 114 d (Table 1, PA1–PA6), as they span the same time period as the TLS surveys. The data following day 114 show little or no additional post-seismic deformation. The vertical post-seismic deformation observed between 17 and 114 d was 13.8 ± 1.1 mm. The maximum horizontal post-seismic deformation observed was 10.1 ± 1.1 mm over the same period. The measurements of vertical and horizontal deformation increase with a decreasing rate over the study period, indicative of afterslip and near-field post-seismic deformation.

4 DISCUSSION

4.1 Surface change detection

We were able to measure the vertical difference between modelled surfaces with an average precision of ∼3 mm. The selection of smooth road surfaces and close proximity to the scanner produced point cloud data sets of high density and low noise. The figure for average precision was obtained mainly due to the use of the DSI interpolation method and the fact that noise within the point cloud, produced by clock-time errors for two-way traveltime, has a Gaussian distribution about the mean, representing a close approximation to the actual surface. The precision of any repeat scan method is dependent on the precision of the scanner as well as the range, roughness and incidence of the surface to be scanned. An important consideration is that the angle of laser incidence on the road surface becomes progressively more acute with increasing range, assuming the scanner is oriented vertical, looking down the road surface. This increase in incidence with range has the effect of degrading the precision of the returns and increasing the point spacing of the acquired data set. Although the Riegl LMS-z420i

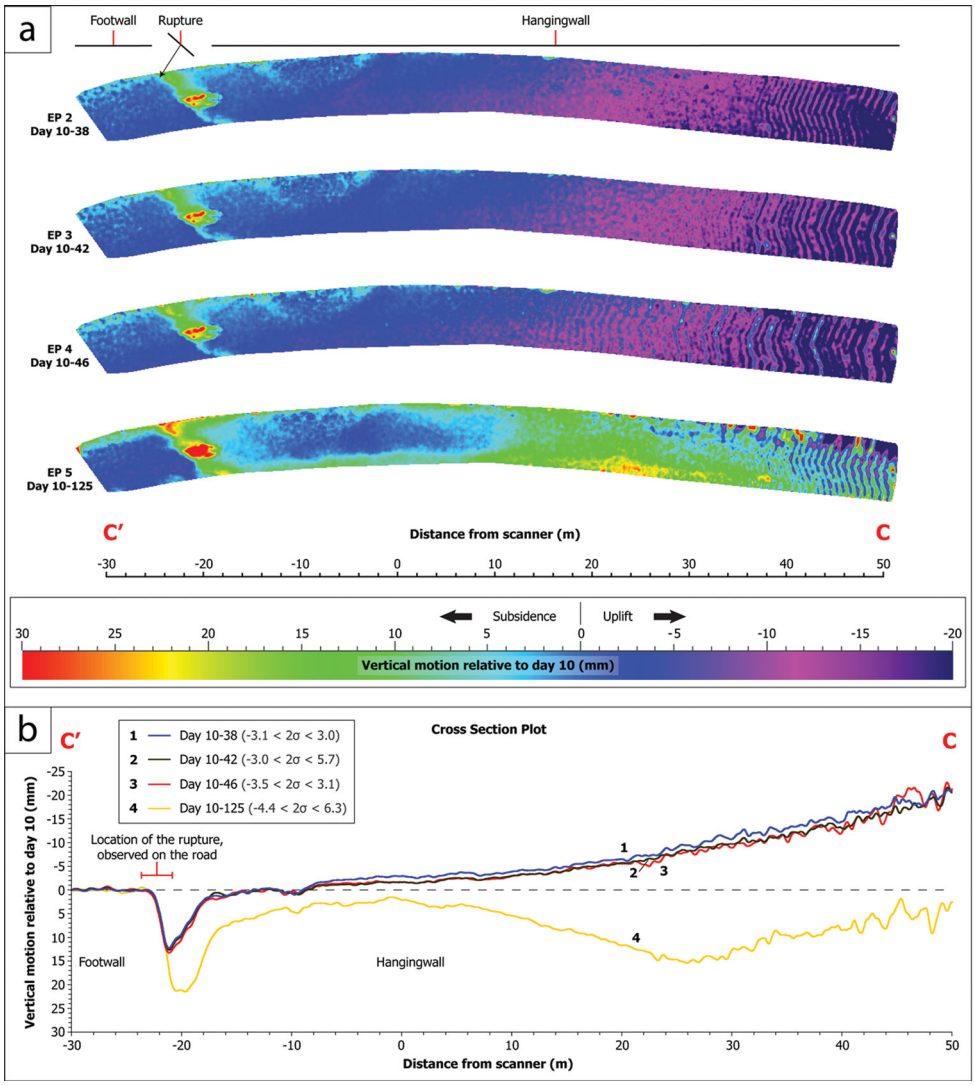

Figure 6. Post-seismic deformation results for site EP. (a) Colour map plot of vertical deformation (mm) in a footwall static reference frame for subsequent TLS data sets, relative to the initial data set acquired at the site. (b) Cross-sectional plot of the surface deformation between C and C' in (a).

has an effective range of 1000 m, we found that due to the effects of reduced incidence at range, repeat scan precision on the order of ∼3 mm could only be obtained for the road sites we selected at distances of up to 50 m. For this study, precisions range from ±1.2 to 8.1 mm (2σ variation of a moving point average based on a rupture parallel moving window of 250 triangle vertices). 'Min $< 2\sigma <$ Max' bounds in Figs 4(b)–7(b) represent the range of certainty in vertical deformation for each cross-sectional plot, which changes along section due to variations in the smoothness of the road. The precision of horizontal deformation measured using the reflector-pair method is ±5.0 mm, due to a precision of ±2.5 mm in the position of a single cylindrical reflector.

4.2 Post-seismic deformation at L'Aquila

Post-seismic surface deformation, including both horizontal and vertical components increased over time at sites PAG, SP, EP and PA (Fig. 8). The rate of deformation declined over our observation period, and is consistent with rate decay laws for afterslip within the fault zone (e.g. Marone *et al.* 1991). In contrast, little deformation, beyond the precision of our method was observed at site TM (Fig. 8d). The location of the five study sites along the Paganica surface rupture (Fig. 2) allowed us to analyse the along-fault distribution of the post-seismic deformation following this earthquake.

The surface expression of rupture afterslip and near-field post-seismic deformation is not consistent along the surface rupture and is highly variable over short distances. The magnitude of the vertical and horizontal components of post-seismic deformation between 8 and 44 d (or the closest measurement dates available at each site) is shown for the five sites in Fig. 9(a). The greatest vertical and horizontal post-seismic deformation over this period occurred at site PAG (22.5 ± 3.3 mm and 16.4 ± 5 mm, respectively), towards the centre of the surface rupture. The observed vertical and horizontal components of post-seismic deformation decrease from site PAG towards sites TM and EP at the NW and SE ends of the rupture, respectively. The vertical and horizontal components of post-seismic deformation between 8 and 126 d (or the closest measurement dates available at each site) is shown for the five sites in Fig. 9(b). The maximum observed vertical and horizontal components of post-seismic deformation are still observed at PAG, with the exception of the horizontal deformation observed at SP. The relative change in the components of post-seismic deformation between 44 and 126 d

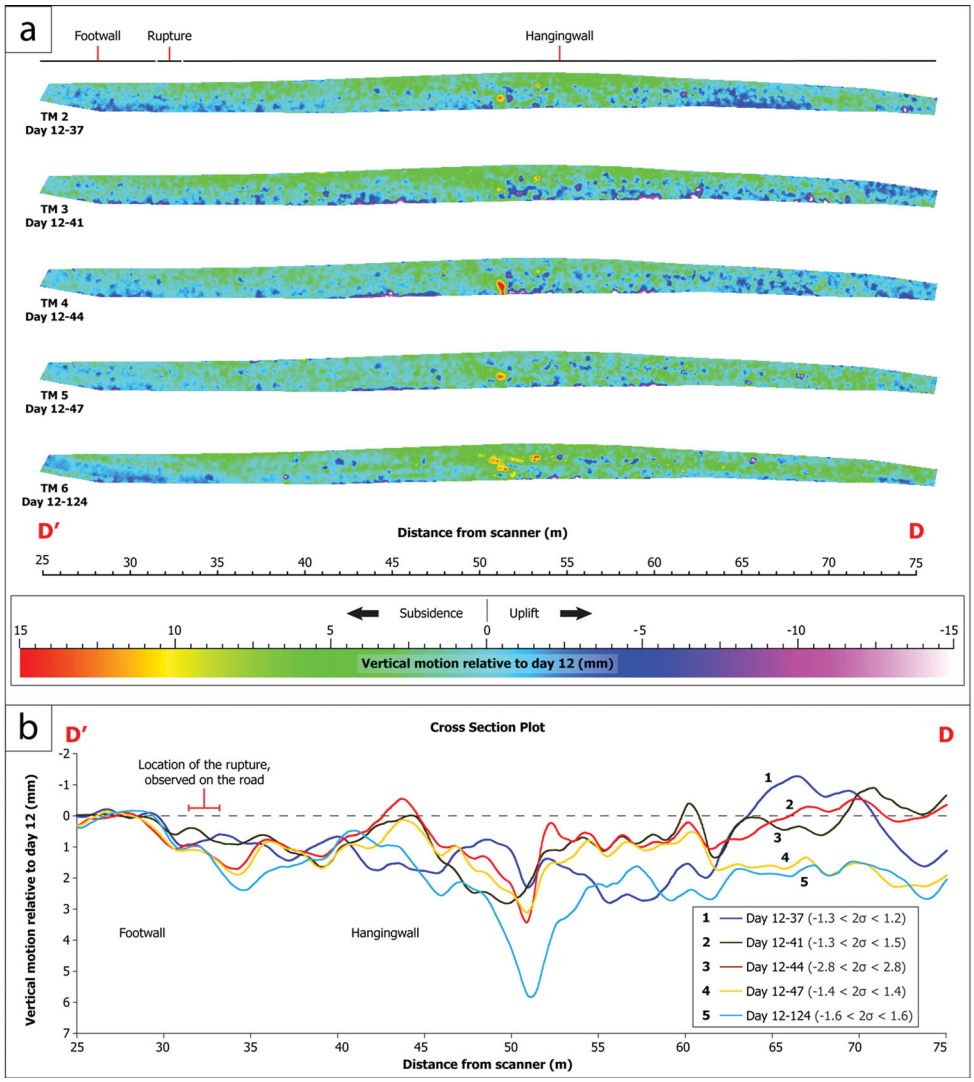

Figure 7. Post-seismic deformation results for site TM. (a) Colour map plot of vertical deformation (mm) in a footwall static reference frame for subsequent TLS data sets, relative to the initial data set acquired at the site. (b) Cross-sectional plot of the surface deformation between D and D' in (a).

is shown in Fig. 9(c). There is a significant increase in deformation over this time period towards the southeastern end of the rupture, observed at sites SP and EP, whereas deformation at TM to the northwest remains low. The vertical and horizontal components of deformation observed at SP increase by 5.4 and 11.1 mm between 42 and 126 d, whereas the vertical and horizontal components of deformation observed at EP increase by 14.2 and 4.4 mm between 42 and 126 d. In comparison the vertical and horizontal components of post-seismic deformation at PAG, towards the centre of the rupture increased by 5.2 and 5.4 mm, respectively.

To illustrate this relative increase in post-seismic deformation at the southeastern end of the rupture, we plotted the maximum observed post-seismic deformation at each site alongside published estimates for the coseismic slip within the fault zone (Fig. 10). The theory of afterslip (Marone *et al.* 1991) dictates that afterslip is driven by coseismic slip deficits (high gradients in coseismic slip) within the fault zone at depth. The unconsolidated material within the fault zone is thought to respond to equilibrate differential shear stresses in the fault zone by the process of gradual creep over time. This behaviour is thought to be responsible for the characteristic decaying rate of afterslip motion observed on surface ruptures. Through the comparison of coseismic and post-seismic fault slip maps produced using far-field GPS data, Cheloni *et al.* (2010) suggested that post-seismic deformation is greatest in regions where shear stress are highest, produced by large gradients in coseismic slip. We plot the coseismic slip within the fault zone sampled at horizontal transects at 1.5 and 3.5 km depth along the length of the fault using values from a modelled coseismic fault slip map inferred from coseismic GPS motions (Cheloni *et al.* 2010; Figs 10a and b). We plot the mean of horizontal and vertical components of the maximum observed post-seismic deformation for each of the five study sites. To directly compare our surface measurements to the modelled coseismic slip within the fault plane, we resolved these magnitudes onto the modelled 54° dipping fault plane, (Table 2, columns 5, 6 and 7 and Fig. 10b, yellow circles). We note that sites SP and EP at the southeastern end of the rupture, where significant increases in post-seismic deformation were observed between 44 and 126 d, are located above a region in the fault zone where the gradient of coseismic slip is high at 3.5 km depth (28 cm change in coseismic slip per km distance along the fault). Sites PA and

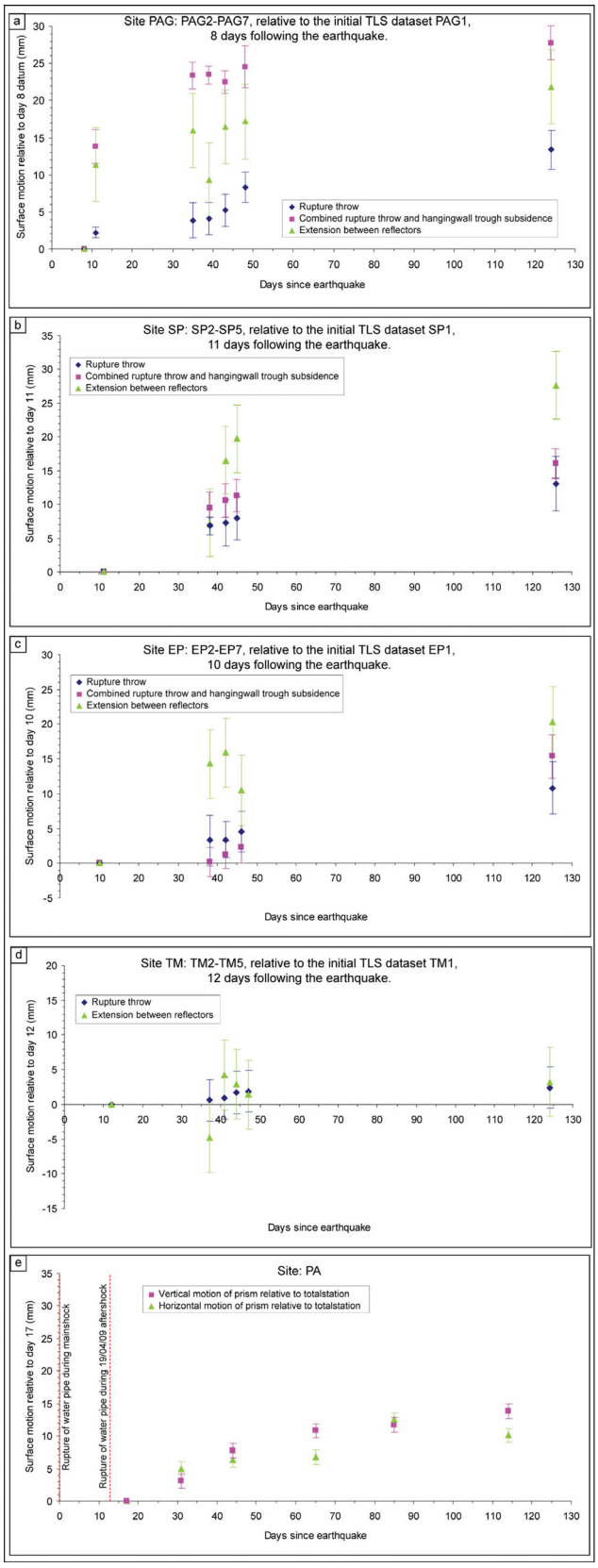

Figure 8. (a–d) Post-seismic deformation measurements for each TLS data set relative to the initial data set, plotted against time since the earthquake. Error bars represent 2σ certainty. (e) Site PA: Horizontal and vertical components of the change in distance between points A0 and A1 (Fig. 3b), relative to the first measurement at day 17.

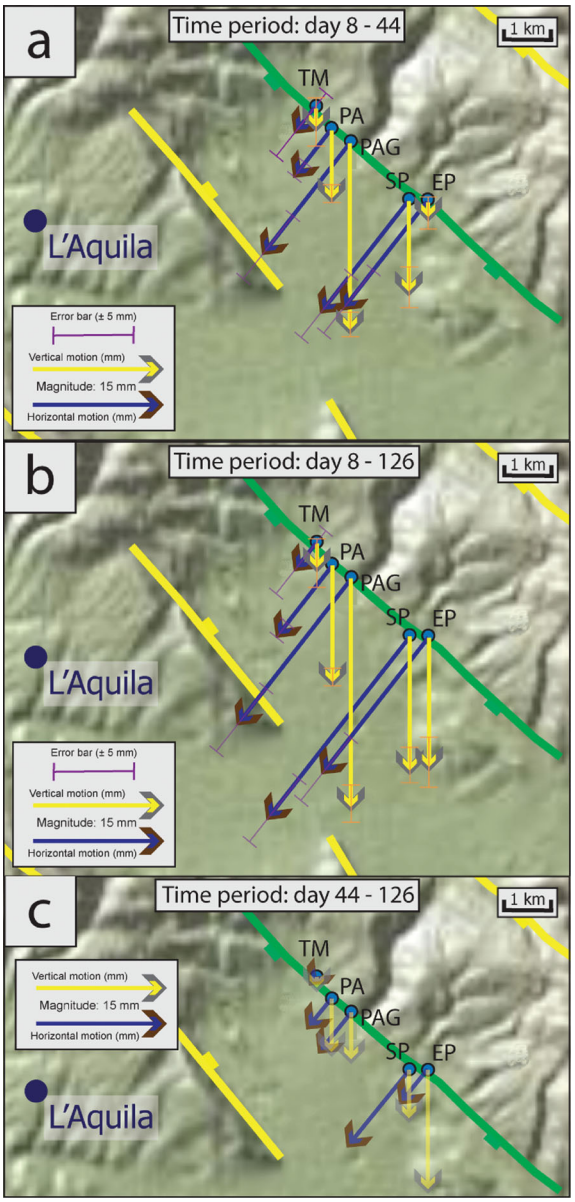

Figure 9. Map distribution of the horizontal and vertical components of post-seismic deformation observed at the five study sites over the period: (a) 8–44 d, (b) 8–126 d and (c) 44–126 d. Arrow lengths and error bars for each measurement scaled from those shown in the legend. The green line represents the inferred subsurface trace of the Paganica fault.

TM which experienced relatively lower values of post-seismic deformation are located above a region where the coseismic slip gradient is of a lesser value at 3.5 km depth (10 cm change in coseismic slip per km distance along the fault). The correlation between the coseismic slip gradient and the increased magnitude of on-rupture post-seismic deformation between 44 and 126 d provides near-field evidence to support the suggestion by Cheloni *et al.* (2010) that post-seismic deformation is driven by high gradients in coseismic slip within the fault zone. A coseismic slip map produced by Atzori *et al.* (2009) from a coseismic interferogram also shows a similar signal of high coseismic slip gradient. We chose not to include this slip map in our analysis as the cell size is slightly greater than the spacing between our sites. The difference in post-seismic deformation between our study sites suggests post-seismic

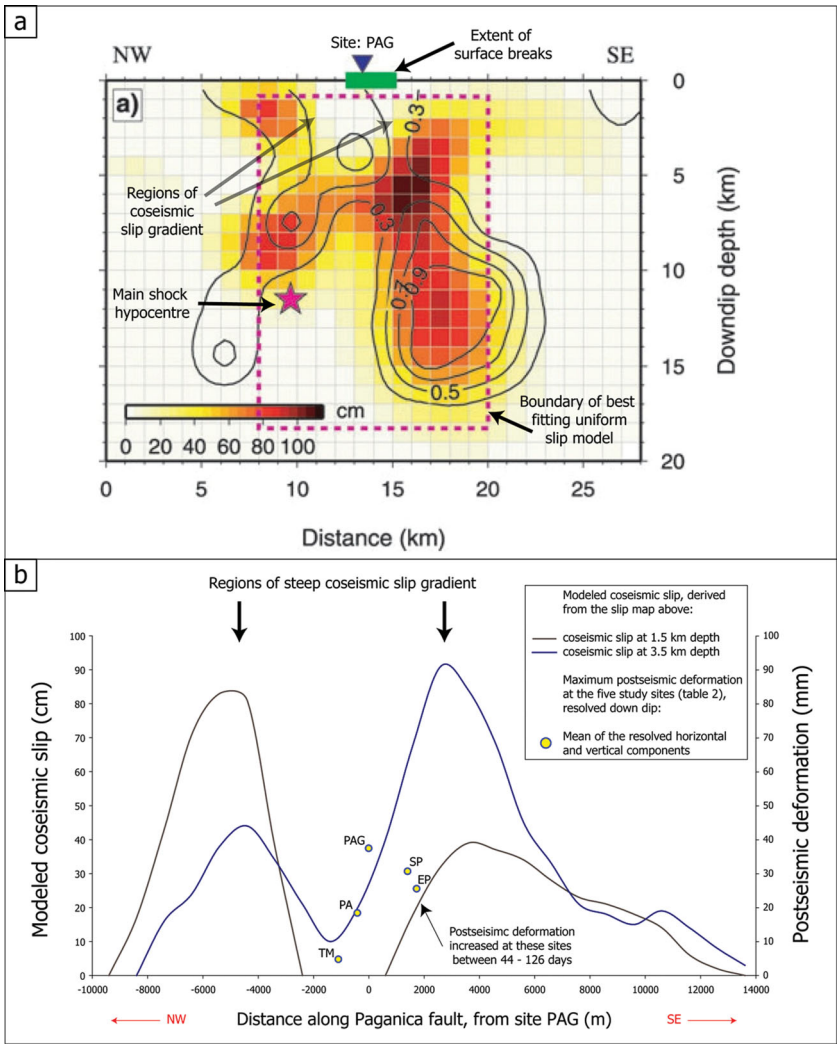

Figure 10. (a) Modelled coseismic fault slip map from Cheloni *et al.* (2010). The contours represent coseismic slip in metres. (b) Plot of the coseismic slip at 1.5 and 3.5 km depth within the fault zone and the maximum observed post-seismic deformation at each study site. The precise positions of peaks in coseismic slip will be affected by the errors estimated through Monte Carlo simulation (see Cheloni *et al.* 2010, supplementary material).

Table 2. The maximum vertical and horizontal components of post-seismic deformation, as observed and resolved as slip in a 54° dipping fault zone.

Site	Survey time frame (days after earthquake)	Maximum observed vertical post-seismic deformation (mm)	Maximum observed horizontal post-seismic deformation (mm)	Maximum observed vertical post-seismic deformation, resolved downdip (mm)	Maximum observed horizontal post-seismic deformation, resolved downdip (mm)	Mean of resolved vertical and horizontal components (mm)
PAG	8–124	27.7	21.8	47.1	26.9	37.0
SP	11–126	16.0	27.6	27.2	34.1	30.7
EP	10–125	15.4	20.3	26.2	25.1	25.7
TM	12–124	2.4	4.2	4.1	5.2	4.7
PA	17–114	13.8	10.1	23.5	12.5	18.0

deformation occurs as a response to a complex pattern of coseismic slip, which produces spatially varying stresses within the fault zone.

The maximum horizontal and vertical components of post-seismic deformation observed in the far field using GPS (Cheloni *et al.* 2010) are 9 mm towards south-southwest (site: AQUI) and 50 mm downward (site: PAGA), respectively (Fig. 1, black arrows). The three areas of maximum line of sight post-seismic displacement (PS, CT and OF) identified by Lanari *et al.* (2010) using SBAS-DInSAR are downward 35, 26 and 18 mm, respectively (Fig. 1, yellow dots, PS, CT and OF). These far-field post-seismic measurements are not significantly greater than the near-field deformation we have measured at sites PAG, PA, SP and EP. This comparison suggests that far-field post-seismic deformation can be attributed to the propagation of near-field post-seismic deformation of similar magnitude. Modelling the propagation of near-field post-seismic deformations into the far field is required to rigorously test this hypothesis, which was beyond the scope of this paper.

5 CONCLUSION

The use of repeat TLS at four sites along the L'Aquila earthquake surface rupture allowed post-seismic deformation on the order of ∼3 mm to be observed at distances of up to 50 m from the laser scanner. The TLS data was complemented by total station data from a fifth site. The measurements of post-seismic deformation from sites PAG, SP, EP and PA show an increase over time with decreasing rate, indicative of afterslip within the fault zone. Surface deformation observed at site TM are within the precision of the method and deemed insignificant. A relative increase in post-seismic deformation was observed between 44 and 126 d at sites SP and EP towards the southeastern end of the rupture. We attribute this increase to a high gradient of coseismic slip within the fault zone beneath these sites and suggest the increase in deformation is driven by increased shear stresses in this part of the fault zone. We note that the magnitude of far-field post-seismic deformation, measured using GPS and InSAR is not significantly greater that the near-field deformation we measured at distances up to 50 m of the rupture. We suggest that localized afterslip within the fault zone, driven by increased shear stresses in regions of high coseismic slip gradient is responsible for the majority of post-seismic deformation on all scales.

ACKNOWLEDGMENTS

Funded by NERC grants NE/H003266/1 and NE/E016545/1 and Durham University Doctoral Fellowship (MW). We thank N. De Paola, A. Yates, A. Bubeck and G. Sileo for assistance in the field, also D. Stevenson and G. Wilkinson for IT support. Two anonymous reviewers and the editor Duncan Agnew are thanked for their thorough comments which greatly improved the manuscript.

REFERENCES

Amoruso, A. & Crescentini, L., 2009. Slow diffusive fault slip propagation following the 6 April 2009 L'Aquila earthquake, Italy, *Geophys. Res. Lett.,* **36,** L24306, doi:10.1029/2009GL041503.

Atzori, S. *et al*., 2009. Finite fault inversion of DInSAR coseismic displacement of the 2009 L'Aquila earthquake (central Italy), *Geophys. Res. Lett.,* **36,** L15305, doi:10.1029/2009GL039293.

Boncio, P., Pizzi, A., Brozzetti, F., Pomposo, G., Lavecchia, G., Di Naccio, D. & Ferrarini, F., 2010. Coseismic ground deformation of the 6 April 2009 L'Aquila earthquake (central Italy, Mw6.3), *Geophys. Res. Lett.,* **37,** L06308, doi:10.1029/2010GL042807.

Cheloni, D. *et al*., 2010. Coseismic and initial post-seismic slip of the 2009 M-w 6.3 L'Aquila earthquake, Italy, from GPS measurements, *Geophys. J. Int.,* **181**(3), 1539–1546, doi:10.1111/j.1365-246X.2010.04584.x.

Degasperi, M., 2010. *Relazione sui monitoraggi nella zona di Paganica*. Provincia Autonoma di Trento, Servizio Geologico, Report Marzo 2010. Available at: http://www.protezionecivile.tn.it/geologico/images/Notizie2010/abruzzo/report_03_2010+ALL.pdf (last accessed 2011 July).

Falcucci, E. *et al*., 2009. The Paganica Fault and surface coseismic ruptures caused by the 6 April 2009 earthquake (L'Aquila, Central Italy), *Seismol. Res. Lett.,* **80**(6), 940–950, doi:10.1785/gssrl.80.6.940.

Gold, P.O. *et al*., 2010. Analyses of coseismic surface rupture from the 4 April 2010 El Mayor-Cucapah earthquake using terrestrial LiDAR, *GSA Abstr. Prog.,* **42**(5), 177.

Kayen, R., Pack, R.T., Bay, S., Sugimoto, S. & Tanaka, H., 2006. Terrestrial-LIDAR visualization of surface and structural deformations of the 2004 Niigata Ken Chuetsu, Japan Earthquake, *Earthq. Spectra J.,* **22**(S1), S147–S162.

Lanari, R. *et al*., 2010. Surface displacements associated with the L'Aquila 2009 Mw 6.3 earthquake (central Italy): new evidence from SBAS-DInSAR time series analysis, *Geophys. Res. Lett.,* **37,** L20309, doi:10.1029/2010GL044780.

Mallet, J.L., 1992. GOCAD: a computer aided design program for geological applications, in *Three Dimensional Modeling With Geoscientific Information Systems*, pp. 123–141, ed. Turner A.K., Kluwer, Netherlands.

Marone, C.J., Scholtz, S.H. & Bilham, R., 1991. On the mechanics of Earthquake Afterslip, *J. geophys. Res. Solid Earth,* **96,** 8441–8452.

Michetti, A.M., Serva, L. & Vittori, E., 2000. Italy hazard from capable faulting, a database of active capable faults of the Italian onshore territory, 32nd Int. Geol. Congress, Rio de Janeiro, August 2000. Internal report of Agenzia Nazionale Protezione Ambiente, Roma (CD).

Roberts, G.P., 2008. Vizualisation of active normal fault scarps in the Apennines, Italy: a key to assessment of tectonic strain release and earthquake rupture, *J. Virtual Explorer,* **30,** 4, doi:10.3809/jvirtex.2008.00197.

Vittori, E. *et al*., 2011. Surface faulting of the April 6th 2009 Mw 6.3 L'Aquila earthquake in central Italy, *Bull. seism. Soc. Am.,* **101,** 1507–1530.

Walters, R.J. *et al*., 2009. The 2009 L'Aquila earthquake (central Italy): a source mechanism and implications for seismic hazard, *Geophys. Res. Lett.,* **36,** L17312, doi:10.1029/2009GL039337.

Wilkinson, M. *et al*., 2010. Partitioned postseismic deformation associated with the 2009 Mw 6.3 L'Aquila earthquake surface rupture measured using a terrestrial laser scanner, *Geophys. Res. Lett.,* **37,** L10309, doi:10.1029/2010GL043099.